Title

SINGLE ATOM IMAGE CONTRAST: CONVENTIONAL DARK FIELD AND BRIGHT FIELD ELECTRON MICROSCOPY

Authors

Chiu, Wah
Glaeser, Robert M.

Publication Date

1973-11-01

Submitted to Journal of Microscopy

LBL-2450
Preprint

SINGLE ATOM IMAGE CONTRAST: CONVENTIONAL DARK FIELD AND BRIGHT FIELD ELECTRON MICROSCOPY

DONNER LABORATORY

Wah Chiu and Robert M. Glaeser

November 1973

Prepared for the U. S. Atomic Energy Commission
under Contract W-7405-ENG-48

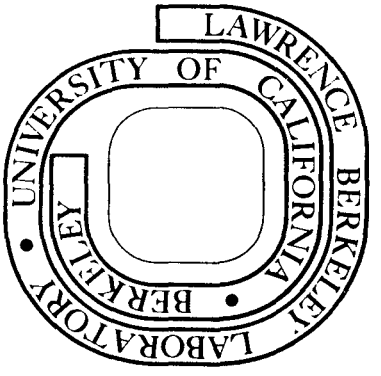

DISCLAIMER

LBL-2450

SINGLE ATOM IMAGE CONTRAST: CONVENTIONAL DARK FIELD AND BRIGHT FIELD ELECTRON MICROSCOPY

Wah Chiu and Robert M. Glaeser
Division of Medical Physics and Donner Laboratory
Lawrence Berkeley Laboratory
University of California, Berkeley, California 94720

SUMMARY

Single atom image intensities are calculated for bright field and various dark field modes, including the ideal beam stop, a wire beam stop, tilted illumination and a displaced aperture. Comparisons of scattering amplitudes and elastic scattering cross sections are made with different object potentials and scattering formulations. The image contrast for one mercury atom (Z = 80) on a column of carbon atoms (Z = 6) as the substrate is also discussed for both the bright field and the various dark field situations. A list of abbreviations to be used in the text is shown below.

ABBREVIATIONS

BF	Bright field
IBS	Ideal beam stop
WBS	Wire beam stop
TI	Tilted illumination
DA	Displaced aperture
u	Ideal central stop radius
w	Wire stop radius
C_s	Spherical abberation coefficient
ΔZ	Defocus
s_f	Aperture radius
RHFS	Relativistic Hartree Fock Slater
HFS	Hartree Fock Slater

INTRODUCTION

The use of high resolution microscopy as a tool to obtain structural information for biological macromolecules has been of great interest to molecular biophysicists. One approach of current interest is the visualization of single heavy atoms that are placed on the macromolecule as a structural label. In this approach, three criteria must be satisfied:

(1) the image mode chosen must provide sufficient contrast,

(2) the method of chemical labeling with heavy atoms must be specific and stable (Beer, 1965), and

(3) it is necessary to eliminate or minimize radiation damage and atomic displacement in the course of observations (Glaeser, 1974).

The latter two problems are still in a very primitive stage of development. Several suggestions have been made as to how one might enhance image contrast:

(1) use image restoration programs that discriminate in favor of heavy atoms (Frank, 1972),

(2) improve the bright field image quality through the use of Fresnel zone plate (Hoppe, 1961, 1963; Eisenhandler & Siegel, 1966),

(3) employ unique image modes with the scanning transmission electron microscope (Crewe et. al. 1970, 1972),

(4) develop "conventional" dark field electron microscopy (Henkelman & Ottensmeyer, 1971; Ottensmeyer et. al., 1973; Hashimoto et. al., 1972, 1973).

In high resolution transmission electron microscopy, phase contrast theory may be used to evaluate the image contrast expected in both bright field and dark field modes of operation. The calculated image intensity profiles are generally dependent upon the choices of object potential, scattering formula and parameters describing the operation of the microscope. In bright field, Eisenhandler and Siegel (1966) calculated the image contrast of single atoms and of linear chains of atoms. Their calculations used only a real atomic scattering amplitude obtained from the 1st Born approximation, and values of spherical abberation coefficient that are unrealistic for the presently available high resolution electron microscope. Improvements were made by Reimer (1969), and by Hall and Hines (1970) who used a complex scattering amplitude, calculated from the WKB method and the partial wave method respectively, to evaluate the bright field image intensity profiles of single atoms and atom clusters. However, no estimate of contrast between the single atoms and the substrate was considered.

Koike and Kamiya (1970) used a scattering formula due to Lenz to calculate dark field image intensity profiles of a single gold atom. These calculations assumed an ideal beam stop in the back focal plane, but this could bear no experimental reality. Calculations by Hashimoto (1972) showed an unusually asymmetric image intensity profile for a single thorium atom in the case of tilted illumination dark field imaging. This result was pointed out by Hashimoto et. al. (1973) to be excessive due to the use of a rectangular aperture in their previous calculations. All of these dark field, single atom calculations were based on the 1st Born approximation, and no consideration of substrate contrast was

taken into account.

The purpose of the present study is to calculate single atom image intensities in bright field and different "conventional", (fixed-beam) dark field image modes with practical values of operational parameters of the microscope. In the dark field case a comparison is made between the ideal beam stop, a realistic wire beam stop, tilted illumination, and the simple use of a displaced aperture. The phase grating approximation is used to calculate the complex scattering amplitude, and an atom object is represented by recent atomic potentials computed for the Relativistic Hartree Fock Slater atomic model (Carlson, et. al. 1970). Contrast values between one mercury atom and a thin layer of linearly aligned carbon atoms are presented in terms of image point intensities. Moreover, the validity of a linear summation of single atom image intensities (and of total elastic scattering cross sections of single atoms) is also discussed.

ASSUMPTIONS

The assumptions in the present calculations are:

(1) the object is illuminated with perfectly coherent plane waves,

(2) atoms are represented by spherically symmetric potentials,

(3) only the elastic scattering is considered,

(4) the phase grating approximation is valid,

(5) the phase distortion in the imaging system is entirely due to defocus and spherical abberation.

It is recognized that efforts must be made in future theoretical work to

relax the first three assumptions.

METHODS OF CALCULATIONS

All numerical computations were carried out on a CDC 7600 computer. The outline of the calculations is indicated in figure 1. The major steps include the calculation of the projected object potential, the scattering amplitude, the total elastic scattering cross section, the output spectrum, the image wave amplitude, and the image intensity. Each mode of "conventional" electron microscopy is characterized by its output spectrum and image intensity formation as described below.

(I) Projected object potential $\phi(\rho)$:

Spherically symmetric potentials of free atoms with atomic number ranging from $Z = 2$ to $Z = 126$, based on Relativistic Hartree Fock Slater wave functions, can be calculated from the radially dependent parameters tabulated by Carlson et. al. (1970). Thomas-Fermi atomic potentials (Ibers and Hoerni, 1954) are also used to calculate the complex scattering amplitude of a single atom, in order to compare with those calculated by Ibers (1968) who used a partial wave scattering formulation. The projected object potential $\phi(\rho)$ on the plane immediately after the object, which in the present calculations is either a single atom or a layer of axially aligned atoms, can be conveniently expressed as equation 1.

$$\phi(\rho) = \sum_{j=1}^{m} p_j \int_0^{\infty} V_j(x_0, y_0, z_0)\, dz \qquad (1)$$

where p_j is the number of atoms with atomic potential $V_j(x_0, y_0, z_0)$, m is the number of different kinds of atoms, and ρ is the radial coor-

dinate in the plane immediately below the object (and normal to the $\hat{z}$ axis, i.e., $\rho = \sqrt{x_0^2 + y_0^2}$).

(II) Scattering amplitude $F_{sp}(\vec{s})$ and $F_{wp}(\vec{s})$:

A complex scattering amplitude, $F_{sp}(\vec{s})$, can be calculated from the phase grating approximation (also known as the strong phase approximation) as expressed in equation 2 (Schiff, 1956):

$$F_{sp}(\vec{s}) = i2\pi/\lambda \int_0^\infty (1 - \exp i\pi\phi(\rho)/\lambda E)\ J_0(2\pi\rho|\vec{s}|)\rho d\rho \qquad (2)$$

To a less accurate degree of approximation, one can start with a real scattering amplitude, $F_{wp}(\vec{s})$, which can be calculated from the weak phase approximation, also known as the 1st Born approximation, (Schiff, 1956):

$$F_{wp}(\vec{s}) = (2\pi^2/\lambda^2 E) \int_0^\infty \phi(\rho)\ J_0(2\pi\rho|\vec{s}|)\rho d\rho \qquad (3)$$

The symbols used in equations 2 and 3 are defined as follows:

λ = the relativistic wavelength of the incident electron;

E = the accelerating voltage;

$|\vec{s}| = |s_x\hat{s}_x + s_y\hat{s}_y| = \frac{2}{\lambda}\sin\frac{\theta}{2}$ (for an angle, θ, of scattering), which is the spatial frequency in the Fourier domain;

J_0 = the zero order Bessel function.

The integrals in equations 1 - 3 were approximated by successive analytical integrations under the central portion of a cubic polynomial, fitted to every four consecutive points of the integrand (Hildebrand, 1956). The sampling distances were set equal to those tabulated by Carlson.

Convergence of integrations was confirmed by using finer sampling intervals; in this case the corresponding atomic potentials were obtained at the intermediate points by a third-order Lagrange interpolation of the values tabulated by Carlson.

(III). Total elastic scattering cross section σ:

The total elastic scattering cross section, σ, can be calculated from the Optical Theorem (Schiff, 1956) as in equation 4:

$$\sigma = 2\lambda \mathrm{Im} \left\{ F_{sp}(0) \right\} . \qquad (4)$$

This represents a rigorously correct value of the total cross section when equation 2 is used to calculate $F_{sp}(0)$, because the phase grating approximation represents an exact summation of the infinite Born series at small scattering angles.

(IV). Phase distortion factor $\gamma(|\vec{s}|)$ and aperture function $A(\vec{s})$:

The phase factor in equation 5 is used to account for the phase distortion due to spherical abberation and defocus. Astimagtism is assumed to be compensated and hence is ignored.

$$\gamma(|\vec{s}|) = \pi/2(-C_s \lambda^3 |\vec{s}|^4 + 2\Delta Z \lambda |\vec{s}|^2) \qquad (5)$$

where C_s is the spherical abberation coefficient and ΔZ is the amount of defocus at the object.

The aperture function defines the shape, size and position of the objective aperture. For the three separate cases of bright field, tilted illumination, and displaced aperture dark field images, the aperture function can be defined according to equation 6:

$$A(\vec{s}) = \begin{cases} 1 & |\vec{s}| \leq s_f \\ 0 & \text{elsewhere} \end{cases} \tag{6}$$

where s_f is the radius of the objective aperture. The aperture function can be defined for the ideal beam stop, dark field case as in equation 7, and for wire beam stop dark field as in equation 8:

$$A(\vec{s}) = \begin{cases} 1 & u < |\vec{s}| \leq s_f \\ 0 & \text{elsewhere} \end{cases} \tag{7}$$

where u is the radius of central beam stop;

$$A(\vec{s}) = \begin{cases} 0 & |\vec{s}| > s_f \text{ and } |s_y| \leq w \\ 1 & \text{elsewhere} \end{cases} \tag{8}$$

where w is the radius of the wire placed along the $\hat{s}_x$ axis of the objective aperture (fig. 2).

The center of coordinates for both the phase factor and the aperture function is dependent upon the mode of operation, and must be represented correctly in the output spectrum. The optimal atom-image patterns are expected to be obtained in different modes of operation when the Scherzer criteria (Eisenhandler and Siegel, 1966) in equation 9a, b are satisfied.

$$(C_s \lambda)^{\frac{1}{2}} \leq \Delta Z \leq (2C_s \lambda)^{\frac{1}{2}} \tag{9a}$$

$$s_f = 1/\lambda(2\Delta Z/C_s)^{\frac{1}{2}} \tag{9b}$$

(V) Output spectrum $\mathcal{O}(\vec{s}, \vec{a}, \vec{b}, \vec{c})$:

The output spectrum is defined in the Fourier domain as a product of the scattering amplitude $F_{sp}(\vec{s} - \vec{a})$, and aperture function

$A(\vec{s} - \vec{b})$ and the phase distortion function $\exp i\gamma(|\vec{s} - \vec{c}|)$, which have respective center of coordinates $\vec{a}$, $\vec{b}$, $\vec{c}$, determined by the chosen mode of microscope operation. In bright field, ideal beam stop, and wire beam stop dark field modes (figure 2), the centers of coordinates of the scattering amplitude, aperture function and phase distortion function are the same and can be set as $\vec{a} = \vec{b} = \vec{c} = 0$. In the titled illumination, dark field case (figure 3), the center of coordinates of the scattering amplitude is shifted along the $\hat{s}_x$ axis with respect to those of the aperture function and phase distortion function, i.e., $\vec{a} = |\vec{a}|\hat{s}_x$ and $\vec{b} = \vec{c} = 0$. In the displaced aperture dark field mode (figure 4), the center of coordinates of the aperture function is shifted along $\hat{s}_x$ with respect to those of the scattering amplitude and phase distortion function, i.e., $\vec{b} = |\vec{b}|\hat{s}_x$, and $\vec{a} = \vec{c} = 0$.

(VI) Image wave amplitude $\psi(\vec{r}_i)$:

The image wave amplitude is calculated by an inverse Fourier transform of the output spectrum for the various modes of operation. In bright field and ideal beam stop, dark field, the circular symmetry of the output spectrum allows us to calculate the inverse Fourier transform as a one dimensional Bessel transform, as represented in equation 10:

$$\psi(\vec{r}_i) = i2\pi\lambda \int_{-\infty}^{\infty} \mathcal{O}(|\vec{s}|)\, J_0(2\pi |\vec{s}|\, |\vec{r}_i|)\, |\vec{s}|\, d|\vec{s}| \quad . \tag{10}$$

In the bright field case the total image wave amplitude is given by $1 + \psi(\vec{r}_i)$, but in the dark field case the function $\psi(\vec{r}_i)$ gives the complete image wave amplitude. In the wire beam stop, tilted illumination, and displaced aperture dark field cases, the image wave amplitudes are evaluated by a two dimensional inverse Fourier transform as in equation 11:

$$\psi(\vec{r}_i) = i \int_{-\infty}^{\infty} \mathcal{O}(\vec{s}, \vec{a}, \vec{b}, \vec{c}) \exp\left(i\, 2\pi(\vec{s} \cdot \vec{r}_i)\right) d\vec{s} \qquad (11)$$

where $\vec{r}_i = x_i\hat{x}_i + y_i\hat{y}_i$. The integration method as described in II was again used to evaluate the one dimensional integral with a sampling distance of 0.01 Å^{-1} for $|\vec{s}| \leq 0.3\ \text{Å}^{-1}$, and of 0.005 Å^{-1} for $|\vec{s}| > 0.3\ \text{A}^{-1}$. Convergence of integration was confirmed by using finer sampling intervals. In the case of the two dimensional integrations, a fast Fourier transform algorithm (Singleton, 1969) was used for a 243×243 square array, with a sampling interval of 0.013 Å^{-1}.

(VII) Image intensity $I(\vec{r}_i)$:

The image intensity is the product of the total image wave amplitude and its complex conjugate. The bright field and the dark field image intensities are thus given by equations 12 and 13 respectively:

$$I_b(\vec{r}_i) = \left(1 + \psi(\vec{r}_i)\right)\left(1 + \psi^*(\vec{r}_i)\right) \qquad (12)$$
$$= 1 + \psi(\vec{r}_i) + \psi^*(\vec{r}_i) + \psi(\vec{r}_i)\ \psi^*(\vec{r}_i)$$

$$I_d(\vec{r}_i) = \psi(\vec{r}_i)\ \psi^*(\vec{r}_i) \quad . \qquad (13)$$

It must be remembered that the wave amplitude, and therefore the image intensity, depends upon $\phi(\rho)$, E, λ, C_s, ΔZ, u, w, s_f, $\vec{a}$, $\vec{b}$, $\vec{c}$, according to the various modes of operation. The present calculations were carried out for single atoms and for layers of atoms of Hg and C, assuming the practical values of E = 100 kV, λ = 0.037 Å, C_s = 1.4 mm; the other parameters are taken as variables. The image intensities are presented by a two dimensional "Z-modulation display" (Grano, 1973) and by profiles along orthogonal orientations. Since each display is chosen to be scaled independently, the relative intensities cannot

show the actual differences in absolute image intensity for the different modes. Information about the absolute intensity for the different situations is contained in the line drawings of the intensity profiles through the center of the atom.

RESULTS AND DISCUSSION

(I) Scattering amplitude and total elastic scattering cross section:

In theory, the phase grating approximation (eq. 2) is superior to the 1st Born approximation, (eq. 3) because the former provides the phase of the scattering amplitude as required by the unitarity principle of quantum mechanics. Table 1 shows that the 1st Born approximation gives a higher magnitude than does the phase grating approximation for the scattering amplitude in the forward direction for a single Hg atom, but there is no difference in magnitude for a single C atom.

Zeitler and Olsen (1964) have previously suggested that the 2nd Born approximation would be as good as the phase grating approximation for describing the scattering by single atoms. Table 2 confirms this numerically by comparing the complex forward scattering amplitudes calculated from the phase grating approximation (eq. 2) to the calculations of Ibers (1968), which were based on the 2nd Born approximation.

Due to the simplicity of the phase grating approximation, the complex scattering amplitudes for single atoms are easily obtained for use in image wave amplitude calculations. Table 3 lists the magnitudes and phases for Hg and C up to a spatial frequency of 1.2 Å^{-1}.

Like the scattering amplitude, the calculated total elastic scattering cross section of a single atom is dependent upon the atomic potential, the accelerating voltage of incident electrons and the scattering formula. Table 4 shows that the elastic scattering cross section calculated here from the phase grating approximation and Relativistic Hartree Fock

Slater atomic potentials (eq. 4) is smaller than that presented by Langmore, Wall and Isaacson (1973) by almost a factor of 2 for Hg but by only a factor of 1.2 for C. These differences are most likely due to their use of the 1st Born approximation, which gives a higher value of scattering amplitude for high Z atom, as evidenced in Table 1, and only secondarily due to the slightly different atomic model.

(II) Bright field (BF) and ideal beam stop (IBS) dark field:

Due to the circular symmetry of the output spectrum in both cases, the image intensities must also be circularly symmetric. The IBS image intensities are far less sensitive to defocus variation in a range of more than 800 Å (fig. 5b) in comparison to the BF image intensities, which actually undergo a reversal of contrast in a range of 800 Å defocus change (fig. 5a). The full width at half maximum is dependent upon defocus and aperture size. Figures 5a, b show that the smallest image width occurs at a defocus of about 800 Å, which is within the range defined by equation 9a; and Table 5 shows that the smallest image width occurs for an aperture radius $s_f = 0.3$ Å^{-1}, which is close to the Scherzer criterion defined by equation 9b. At optimal defocus and aperture size, the image width for BF is about 2.7 Å (fig. 5a), and that for IBS is about 1.7 Å (fig. 5b). The present results of IBS agree qualitatively with those of Koike and Kamiya (1970), though the atom potential and the scattering formula are different. This shows that the qualitative features of an atom image pattern are quite independent of the choice of atomic scattering amplitude of a spherically symmetric object. A plausible explanation of the differences in atom image patterns between BF and IBS may be that in BF, the image is predominantly determined by $\{\psi(\vec{r}_i) + \psi^*(\vec{r}_i)\}$ as in equation

12, whereas in IBS, the image is determined by $\psi(\vec{r}_i)\ \psi^*(\vec{r}_i)$ as in equation 13. The difference in image width is easily understood on the basis of the sharpening that occurs when a bell-shaped function is squared, but the relative sensitivity to defocus is not so easy to explain.

(III) Wire beam stop (WBS) dark field:

Since the output spectrum is centro-symmetric, the atom image intensity also preserves the same symmetry, as shown in figure 6. It is seen in figure 6 that as the wire radius is increased from (a) 0.8μ, to (b) 6μ, and then up to (c) 11μ (for the objective focal length of 1.6 mm), the Hg atom image intensity would become less localized, and would also deviate further from circular symmetry. For a very thin wire of radius 1.8μ, which is still experimentally available, the image intensities are very similar to those of IBS (fig. 7). Hg image profiles along orthogonal directions are shown in figures 7a, b, where it can be seen that the image width is slightly broader along the direction of the wire, and also that the image intensity is again quite insensitive to defocus variation in a range of 800 Å. It is found in Table 5 that the smallest image width can again be found with the optimal aperture radius, as defined in equation 9b. For optimal conditions, the average image width is about 1.8 Å, which is very close to that of IBS.

(IV) Tilted illumination (TI) dark field:

The atom image intensity is symmetric with respect to an axis parallel to the direction of tilting, as shown in figure 8. The variation of tilting angle is represented by different vector positions of the center of coordinates of the scattering amplitude. Variation of $|\vec{a}|$ from 0.34

$Å^{-1}$ to 0.82 $Å^{-1}$ (these correspond to the tilting angles between 1.3×10^{-2} and 3.1×10^{-2} radians for a 35 micron diameter aperture, focal length of 1.6 mm, and E = 100 kV) does not seem to have a significant effect on the image pattern (fig. 8a-d), except for the fact that the intensity is ~4 times higher for the smaller tilting angle. The criteria expressed in equations 9a, b are again found to be the optimal conditions to give an atom image with the smallest image width and the highest peak intensity. The Hg intensity profiles in figure 9a and b once more show the insensitivity to defocus variations in a range of 800 Å, and an image width of about 1.7 Å for the optimal conditions.

(V) Displaced aperture (DA) dark field:

The atom image intensity is now symmetric with respect to an axis parallel to the direction of aperture displacement. By varying the defocus and aperture size, there is no improvement of the broad distribution of the image intensity along the direction of the aperture displacement (fig. 10a, b). This broadening may be due to the asymmetric contributions of the scattering amplitude and the phase distortion function included in the aperture, and also due to the rapid oscillations of the phase distortion function at high spatial frequency.

CONTRAST BETWEEN Hg ATOM AND C SUBSTRATE

Contrast can be defined as the difference between the intensity for the specimen plus substrate and the intensity for the substrate, divided by the average of the two. The effect that the carbon substrate has on the image contrast is taken into account, in a first degree of

approximation, by assuming that the carbon atoms are linearly aligned, parallel to the optical axis. In a model of one Hg atom and a column of n carbon atoms, the contrast (C_1) in the dark field images has been approximated by equation 14:

$$C_1 = \frac{I_{Hg}}{(I_{Hg} + 2 \times n \times I_C)/2} \tag{14}$$

This approximate measure of the contrast in different modes of dark field, for optimal defocus and aperture size, is given in Table 6. These data demonstrate that

(1) the contrast of WBS is very close to that of IBS provided that the wire diameter is sufficiently small,

(2) the contrast of TI is the best of the four modes, and

(3) it seems that contrast remains excellent even when the substrate has a thickness of 40 carbon atoms in all modes of dark field imaging.

The approximation to the contrast, which is defined in equation 14, is based on the assumption that the total image intensity of a column of atoms is the sum of the image intensity for single atoms. This approximation cannot be expected to hold when the object potential is large enough to cause multiple scattering processes to be important, or when other interparticle interference effects are important. Hence, a more accurate approach is to define a contrast, C_2, as in equation 15:

$$C_2 = \frac{I_{Hg+nC} - I_{nC}}{\frac{1}{2}(I_{Hg+nC} + I_{nC})} \tag{15}$$

Here I_{Hg+nC} is the image intensity calculated from the projected object potential with 1 Hg and n carbon atoms by setting the parameters in equation 1 as $m = 2$, $p_1 = 1$, $p_2 = n$, $V_1(x_0, y_0, z_0)$ for Hg atomic potential and $V_2(x_0, y_0, z_0)$ for carbon atomic potential; and I_{nC} is the image intensity calculated from the projected object potential of n carbon atoms with the parameters in equation 1 as $m = 1$, $p_1 = n$, and $V_1(x_0, y_0, z_0)$ for carbon atomic potential. The magnitudes of the forward scattering amplitude of an atom layer are shown in Table 7. It is clear that they are not integral multiples of that for a single atom. This is due to the fact that the scattering amplitude is not linearly proportional to the projected object potential in the phase grating approximation. Moreover, due to the relationship between the total elastic scattering cross section and the forward scattering amplitude (the Optical Theorem), the total elastic scattering cross section of the atom layer is also not linearly related to that of a single atom, as is shown in Table 7.

The image intensity profiles for BF and IBS are calculated with various n. It is found that the image width of an atom layer is very close to that of the single atom when the microscope parameters are the same. It must be recognized that the increasing range of defocus for layers of increasing thickness cannot be taken into account with the phase grating approximation, and this must introduce some error in the results. Contrast calculated for BF and IBS according to equation 15 is given in Table 8 for different n. The results show that

(1) except when n = 1, C_2 is smaller than C_1,

(2) at high n, C_2 differs from C_1 by an increasingly larger factor, for example there is a factor of 3 difference when

n = 20, and

(3) the contrast of IBS is 3 to 8 times higher than that of BF. However, the values of contrast in Table 6 appear to be quite valid when n is sufficiently small.

CONCLUSION

In order to compare atom images in various modes of "conventional" transmission electron microscopy, it is important to consider the three related parameters of full width at half maximum, maximum point intensity in dark field or minimum point intensity in bright field, and contrast. It has been shown that the image width under optimal conditions for bright field is about 1 Å greater than for the various dark field conditions, with the exception of the displaced aperture dark field mode. Bright field images are also found to be far more sensitive to defocus variation than are dark field images. In terms of contrast for the model of 1 Hg and n carbon atoms, the bright field image is far worse than any of the dark field modes.

The image width for the dark field modes (except the displaced aperture) is ~1.7 - 2.0 Å at optimal conditions, which are the same as those given by Scherzer for the bright field image. The contrast for the tilted illumination, dark field case is slightly better than for the other modes of dark field imaging. However, the peak image intensity for the wire beam stop dark field case is about 1.5 higher than that for the case of tilted illumination. Furthermore, image symmetry properties are unique in each mode of dark field, as governed by the symmetry of their respective output spectrum. It is found in the WBS that the image in-

tensity distribution is quite sensitive to the wire thickness. This demonstrates the importance of choice of wire diameter as an experimental consideration.

The insensitivity with variation of tilting angles of the atom image patterns in TI may be used as a justification for assuming perfect coherence in the dark field calculations. Experimentally, electrons are emitted from different points of an electron gun and the final image is a superposition of all images contributed from each point of emission. However, the similarity of image patterns produced from various points of illumination suggests that there would be little distortion of the final image due to the experimental requirement of a finite, extended source.

The scattering amplitude and the total elastic scattering cross section are strongly dependent upon the projected potential and the scattering formula. A close agreement has been found between the phase grating approximation and the 2nd Born approximation for scattering by a single atom, while a significant difference occurs between the phase grating approximation and the 1st Born approximation when the object is a heavy atom or when the object potential is comparable to, or greater than, that of a single heavy atom. In the simple model of 1 Hg and n carbon atoms, it has been shown that it is important to use the proper scattering formula in estimating contrast, even when n is quite small (i.e., n = 7). Since the scattering amplitude is not linearly proportional to the projected object potential, the resultant image intensity (or total elastic scattering cross section) of a layer of atoms is not an integral multiple of the image intensity (or total elastic scattering cross section) of a single atom. However, it is also recognized that

our approximation, in which the carbon atoms of the substrate are aligned in a single column, would probably represent a "worst case" with respect to the non-linear behavior of the elastic scattering cross section and of the image intensity.

In order to estimate contrast corresponding to a more realistic, experimental situation when single Hg atoms are supported by a thin amorphous carbon film, the projected object potential for the substrate must be determined experimentally. Such work is in progress at the authors' laboratory in order to take into full account all experimental conditions and so to provide a realistic, theoretical estimate of image contrast.

REFERENCES

(1) Beer, M. (1965) Laboratory Investigation 14, 6, 1020.

(2) Carlson, T. A., Lu, C. C., Tucker, T. C., Nestor, C. W. & Malik, F. B. (1970) Oak Ridge National Laboratory Report No. 4614.

(3) Crewe, A. V., Wall, J. & Langmore, J. P. (1970) Science 168, 1338.

(4) Crewe, A. V., (1972) Proc. 5th European Cong. on Electron Microscopy 640.

(5) Eisenhandler, C. B. & Siegel, B. M. (1966) J. Appl. Phys. 37, 1613.

(6) Frank, J. (1972) Biophys. J. 12, 484.

(7) Glaeser, R. (1974) in "Electron Microscopy and Microbeam Analysis" Siegel, B. M. ed., John Wiley & Sons.

(8) Grano, D. (1973) private communication.

(9) Hall, C. R. & Hines, R. L. (1970) Phil. Mag. 21, 1175.

(10) Hashimoto, H. (1972) Proc. 30th Ann. EMSA Meeting, 554.

(11) Hashimoto, H., Kumao, A., Hino, K., Endoh, H., Yotsumoto, H., & Ono, A. (1973) J. Electron Microscopy 22, 2, 123.

(12) Henkelman, R. M. & Ottensmeyer, F. P. (1971) Proc. Nat. Acad. Sci., U.S.A. 68, 3000.

(13) Hildebrand, F. B. (1956) Introduction to Numerical Analysis, N. Y., McGraw Hill.

(14) Hoppe, W. (1961) Naturwiss. 48, 736.

(15) Hoppe, W. (1963) Optik 20, 599.

(16) Ibers, J. A. & Hoerni, J. A. (1954) Acta Cryst. 7, 405

(17) Ibers, J. A. (1968) International Tables for X-Ray Crystallography, 3, 216, Kynoch Press, Birmingham, England.

(18) Koike, H. & Kamiya, Y. (1970) 7th Intl. Cong. E. M. 1, 27.

(19) Langmore, J. P., Wall, J. & Isaacson, M. (1973) Optik 38, 335.

(20) Ottensmeyer, F. P., Schmidt, E. E. & Olbrecht, A. J. (1973) Science 179, 175.

(21) Reimer, L. (1969) Z. Naturf, A 24, 377.

(22) Schiff, L. I. (1956) Phys. Rev. 103, 443.

(23) Singleton, R. C. (1969) IEEE Transactions on Audio and Electroacoustics, AU-17, 2, 93.

(24) Zeitler, E. & Olsen, H. (1964) Phys. Rev., A, 136, 1546.

Table 1: Forward scattering amplitude for the phase grating approximation and the 1st Born approximation at 100 kV with RHFS atomic potentials for Hg (Z=80) and C (Z=6).

		Phase grating approximation	1st Born approximation
Magnitude (Å)	Hg	10.09	11.04
	C	2.66	2.66
phase (rad)	Hg	0.24	-
	C	0.032	-

Table 2: Magnitudes and phases of forward scattering amplitude for the phase grating approximation and the 2nd Born approximation at E = 40 kV, with Thomas - Fermi atomic potentials for Hg and C.

		Phase grating approximation	2nd Born approximation*
Magnitude (Å)	Hg	15.87	16.4
	C	7.42	7.9
phase (rad)	Hg	0.266	0.27
	C	0.029	0.03

*Values obtained from Ibers (1968)

Table 3: Magnitudes and phases of scattering amplitudes for Hg and C in the strong phase approximation of 100 kV, with RHFS potentials.

Spatial frequency ($Å^{-1}$)		0	0.05	0.1	0.15	0.2	0.25	0.3	0.35	0.4	0.45	0.5	0.55	0.6	0.65	0.7	0.75	0.8	0.85	0.9	0.95	1.0	1.05	1.1	1.15	1.20
Magnitude (Å)	Hg	10.09	9.99	9.74	9.34	8.85	8.30	7.74	7.19	6.66	6.16	5.70	5.27	4.88	4.53	4.21	3.91	3.65	3.40	3.18	2.98	2.79	2.63	2.47	2.33	2.19
	C	2.66	2.63	2.54	2.41	2.25	2.07	1.88	1.70	1.53	1.37	1.23	1.10	0.99	0.89	0.80	0.72	0.65	0.59	0.53	0.49	0.45	0.41	0.38	0.35	0.32
phase (rad)	Hg	0.237	0.239	0.245	0.255	0.267	0.283	0.300	0.320	0.342	0.364	0.388	0.413	0.439	0.466	0.493	0.520	0.548	0.577	0.606	0.635	0.664	0.693	0.722	0.751	0.781
	C	0.032	0.032	0.033	0.035	0.037	0.039	0.043	0.046	0.050	0.054	0.058	0.063	0.068	0.073	0.078	0.083	0.088	0.093	0.099	0.104	0.109	0.114	0.119	0.124	0.129

Table 4: Total elastic scattering cross section σ at E = 100 kV with different atomic potentials and scattering approximations.

Atomic potentials	scattering approximations	σ ($Å^2$)	
		C	Hg
RHFS	phase grating	0.0064	0.17
HFS*	1st Born	0.0078	0.31

*Values obtained from Langmore, Wall, Isaacson (1973).

Table 5: Full width at half maximum (Å) of Hg image intensities for bright field, ideal beam stop ($u = 0.03$ Å^{-1}) and wire beam stop modes ($w = 0.03$ Å^{-1}) as a function of aperture radius (s_f), with $\Delta Z = 825$ Å.

	s_f(Å^{-1})	0.17	0.2	0.3	0.4	0.5
image width Å	BF	4.4	3.9	2.7	2.8	2.9
	IBS	3.1	2.5	1.8	1.8	1.9
	WBS	3.1	2.3	1.8	1.9	2.0

Table 6: Approximate measure of dark field contrast (C_1) between 1 Hg and n carbon atoms. E = 100 kV, C_s = 1.4 mm, s_f = 0.3 $Å^{-1}$, ΔZ = 825 Å, u = w = 0.03 $Å^{-1}$, $|\vec{a}|$ = 0.4 $Å^{-1}$(TI), $|\vec{b}|$ = 0.34 $Å^{-1}$(DA) for the different modes of dark field.

Number of Carbon Atoms (n) / mode	1	3	7	10	20	40
IBS	1.77	1.44	1.04	0.87	0.55	0.32
WBS	1.77	1.44	1.05	0.87	0.56	0.32
TI	1.81	1.53	1.16	0.98	0.65	0.38
DA	1.77	1.44	1.05	0.87	0.56	0.32

Table 7: Magnitudes of forward scattering amplitudes $|F_{sp}(0)|$ and total elastic scattering cross sections (σ) for a column of n carbon atoms at E = 100 kV.

n	1	3	7	10	16	20	40
$\|F_{sp}(0)\|$ (Å)	2.6	7.9	17.8	24.4	35.8	42.1	65.3
σ (Å^2)	6.40×10^{-3}	5.59×10^{-2}	0.28	0.51	1.02	1.37	2.81

Table 8: Contrast (C_2) between 1 Hg and n carbon atoms in bright field and in ideal beam stop modes. E = 100 kV, ΔZ = 825 Å, s_f = 0.3 $Å^{-1}$, and u = 0.03 $Å^{-1}$.

n	1	3	7	10	20	40
BF	0.15	0.14	0.11	0.09	0.04	0.02
IBS	1.83	1.29	0.67	0.44	0.17	0.10

FIGURE CAPTIONS

Fig. 1. Block diagram of image intensity calculations.

Fig. 2. (a) Schematic diagram for wire beam stop dark field microscopy. The following designations are used: (—·——) for the optical axis, (– – – – –) for the unscattered electrons, and (————) for the scattered electrons.
(b) One dimensional profile of scattering amplitude $|F_{sp}(\vec{s})|$ along $\hat{s}_y$ in the aperture plane with the aperture radius s_f and the wire radius w.

Fig. 3. (a) Schematic diagram for tilted illumination dark field microscopy. The following designations are used: (—·——) for the optical axis, (– – – –) for the unscattered electrons, (————) for the scattered electrons.
(b) One dimensional profile of scattering amplitude $|F_{sp}(\vec{s})|$ along $\hat{s}_x$ in the aperture plane with the aperture diameter $2s_f$ and the extent of tilting $|\vec{a}|$.

Fig. 4. (a) Schematic diagram for displaced aperture dark field microscopy. The following designations are used: (—·——) for the optical axis, (– – – –) for the unscattered electrons, (————) for the scattered electrons.
(b) One dimensional profile of scattering amplitude $|F_{sp}(\vec{s})|$ along $\hat{s}_x$ in the aperture plane with the aperture diameter $2s_f$ and the extent of aperture displacement $|\vec{b}|$.

Fig. 5. Hg image intensities at 100 kV, C_s = 1.4 mm, s_f = 0.3 $Å^{-1}$ for (a) BF (b) IBS with u = 0.03 $Å^{-1}$ at indicated ΔZ. Image intensity reversal occurs within 800 Å defocus range for BF but not for IBS.

Fig. 6. Z-modulation display of Hg image intensities of WBS at 100 kV, C_s = 1.4 mm, s_f = 0.3 $Å^{-1}$, ΔZ = 825 $Å^{-1}$, with different wire radius (a) w = 0.013 $Å^{-1}$, (b) w = 0.103 $Å^{-1}$ (c) w = 0.180 $Å^{-1}$.

The image pattern deteriorates as the wire thickness is increased.

Fig. 7. Hg image intensity profiles of WBS at 100 kV, C_s = 1.4 mm, s_f = 0.3 $Å^{-1}$, w = 0.03 $Å^{-1}$ with indicated ΔZ (a) along the direction of wire (b) normal to the direction of wire. The WBS image intensities are insensitive to defocus variation.

Fig. 8. Z-modulation display of Hg image intensities of TI at 100 kV, C_s = 1.4 mm, s_f = 0.3 $Å^{-1}$, ΔZ = 825 Å, with different tilting angles (a) $|\vec{a}|$ = 0.34 $Å^{-1}$ (b) $|\vec{a}|$ = 0.4 $Å^{-1}$ (c) $|\vec{a}|$ = 0.61 $Å^{-1}$ (d) $|\vec{a}|$ = 0.82 $Å^{-1}$. The image pattern is not much affected by different tilting angles.

Fig. 9. Hg image intensity profiles of TI at 100 kV, C_s = 1.4 mm, s_f = 0.3 $Å^{-1}$, $|\vec{a}|$ = 0.4 $Å^{-1}$ with indicated defocus (a) along the direction of tilting (b) normal to direction of tilting. The image intensities are insensitive to defocus variation.

Fig. 10. Hg image intensity of DA at 100 kV, C_s = 1.4 mm, s_f = 0.3 $Å^{-1}$, ΔZ = 825 Å, $|\vec{b}|$ = 0.34 $Å^{-1}$ (a) along displacement direction (— — —), and normal to displacement direction (———) (b) Z-modulation display. The image width is very broad along the direction of displacement of the aperture.

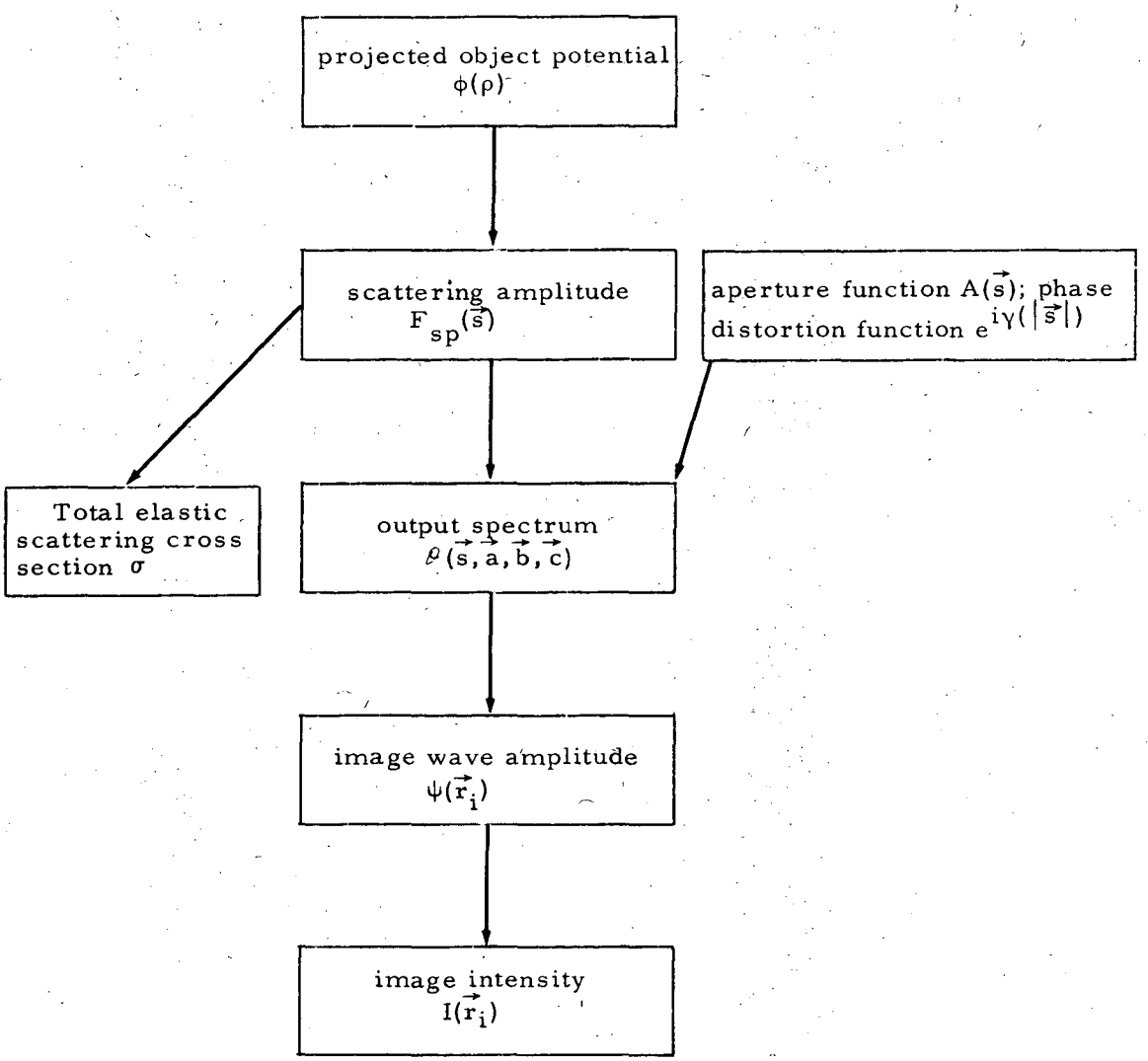

XBL 743-534

Figure 1

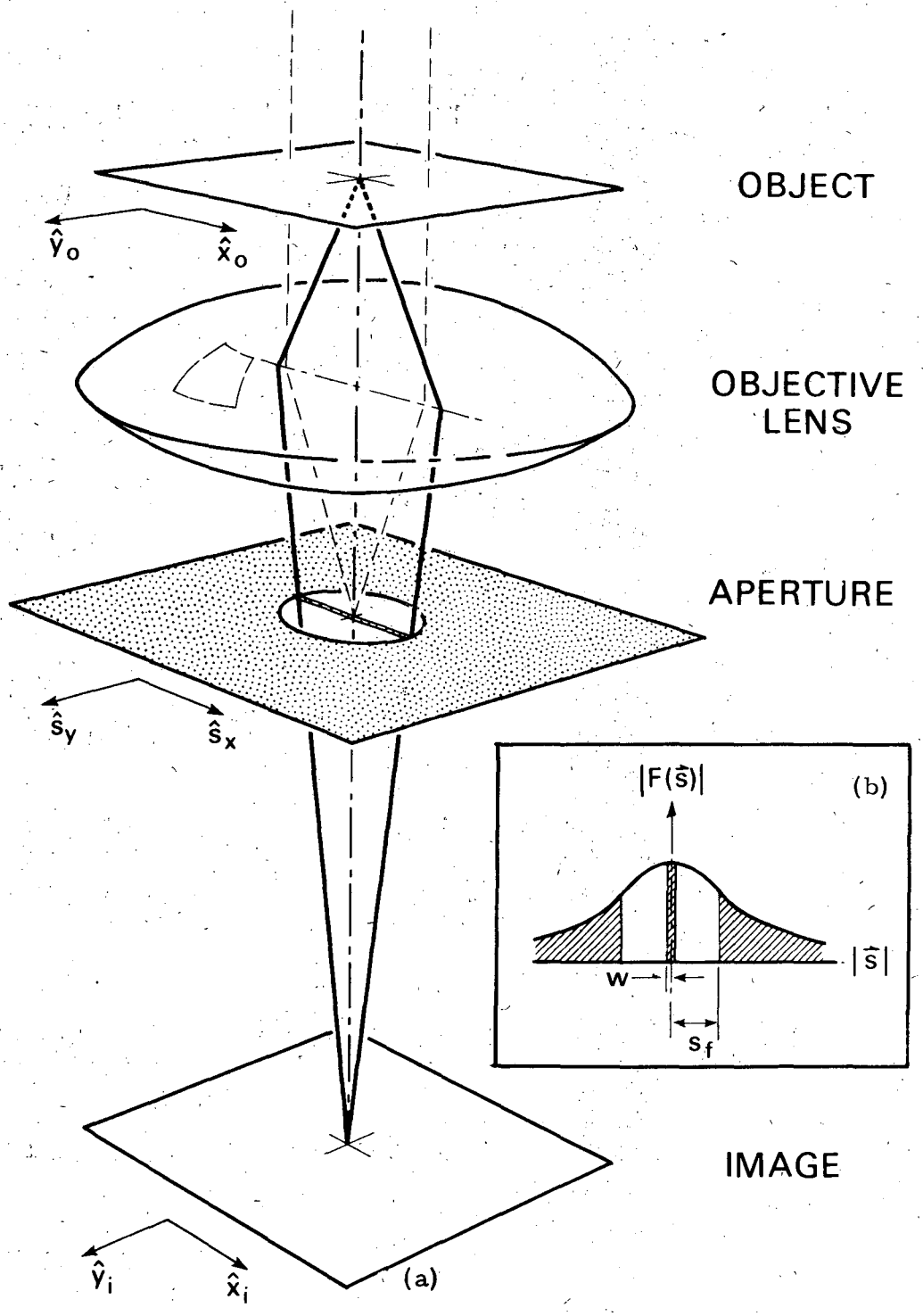

DBL 741-4625

Figure 2

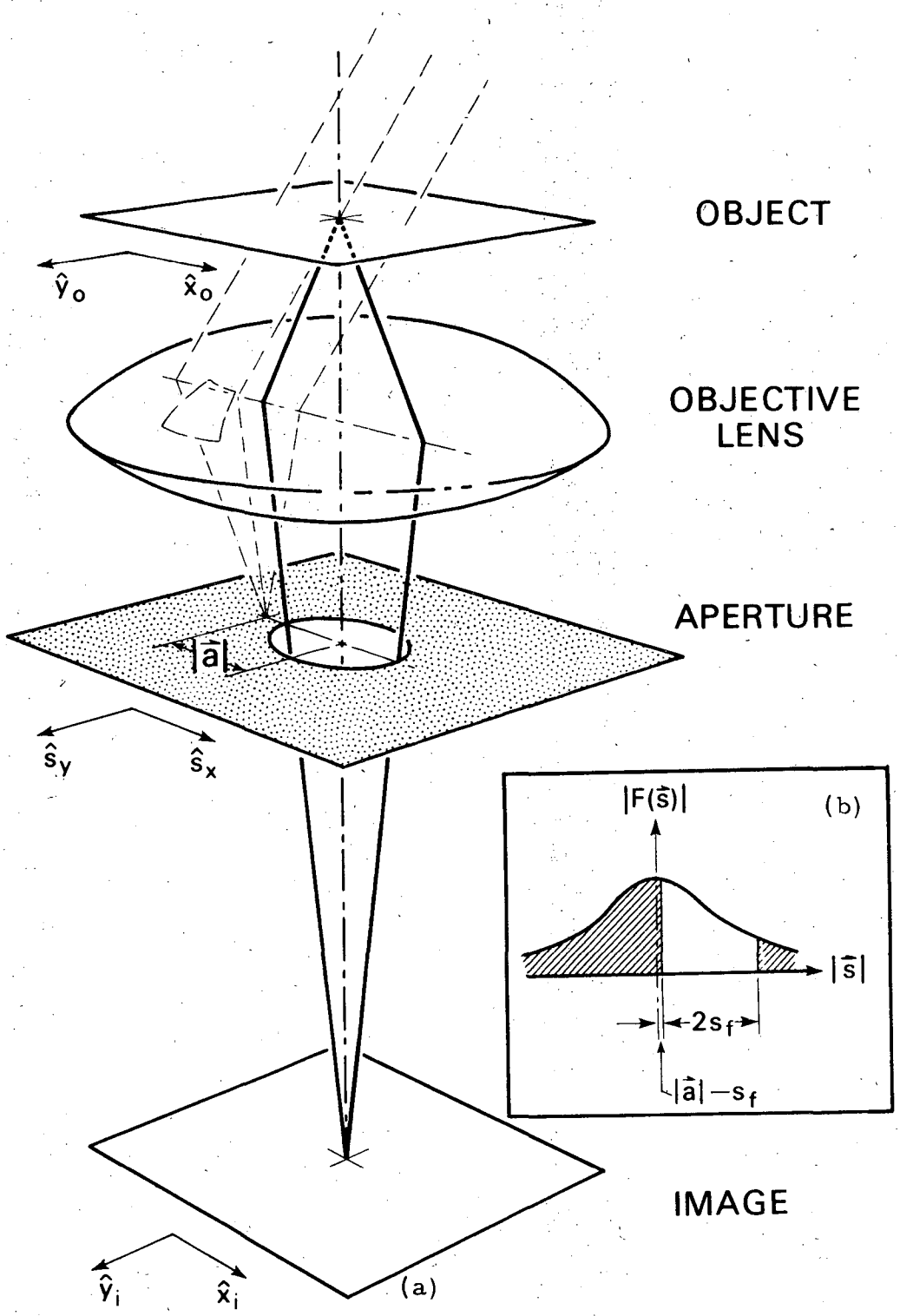

DBL 741-4626

Figure 3

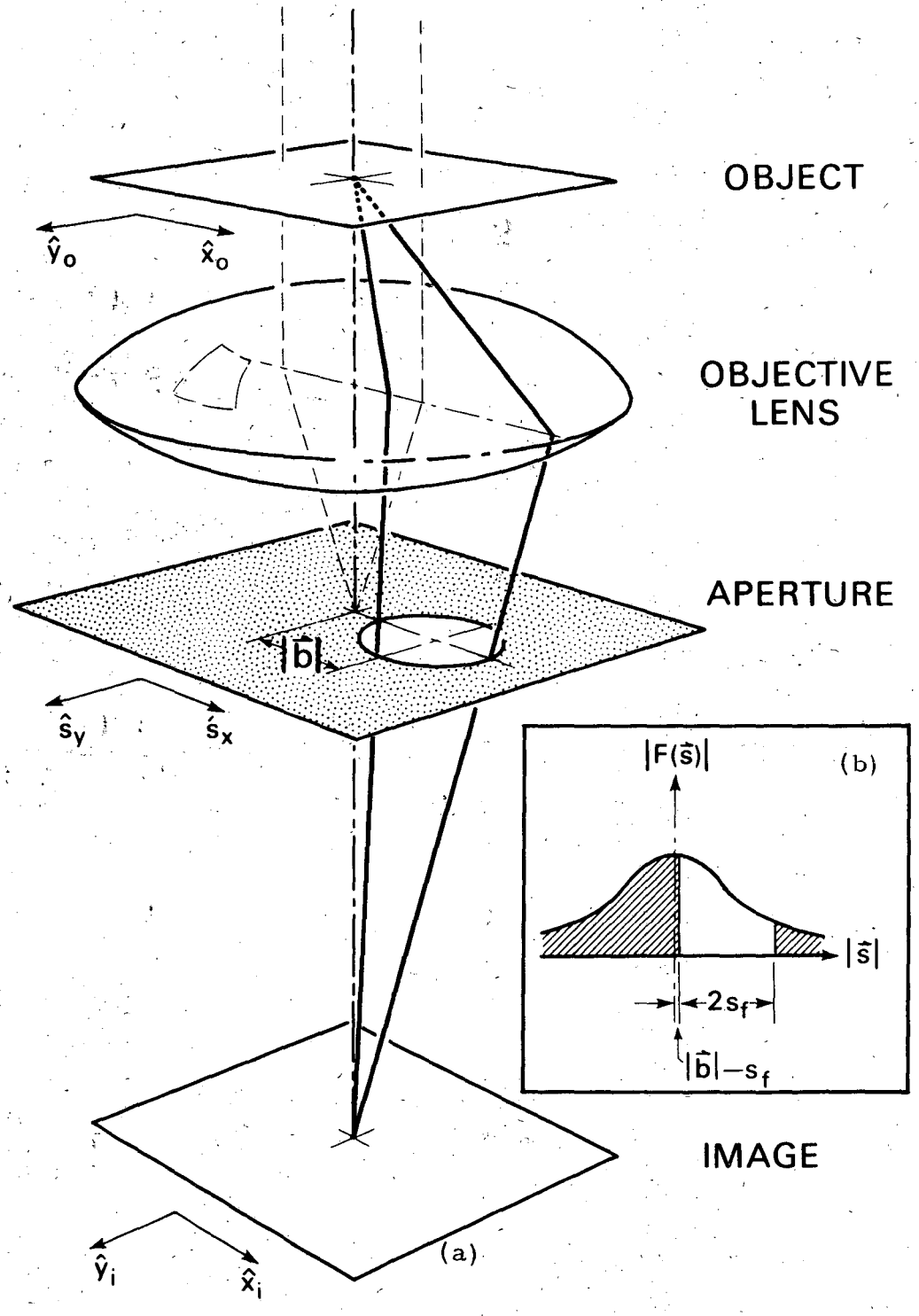

DBL 741-4627

Figure 4

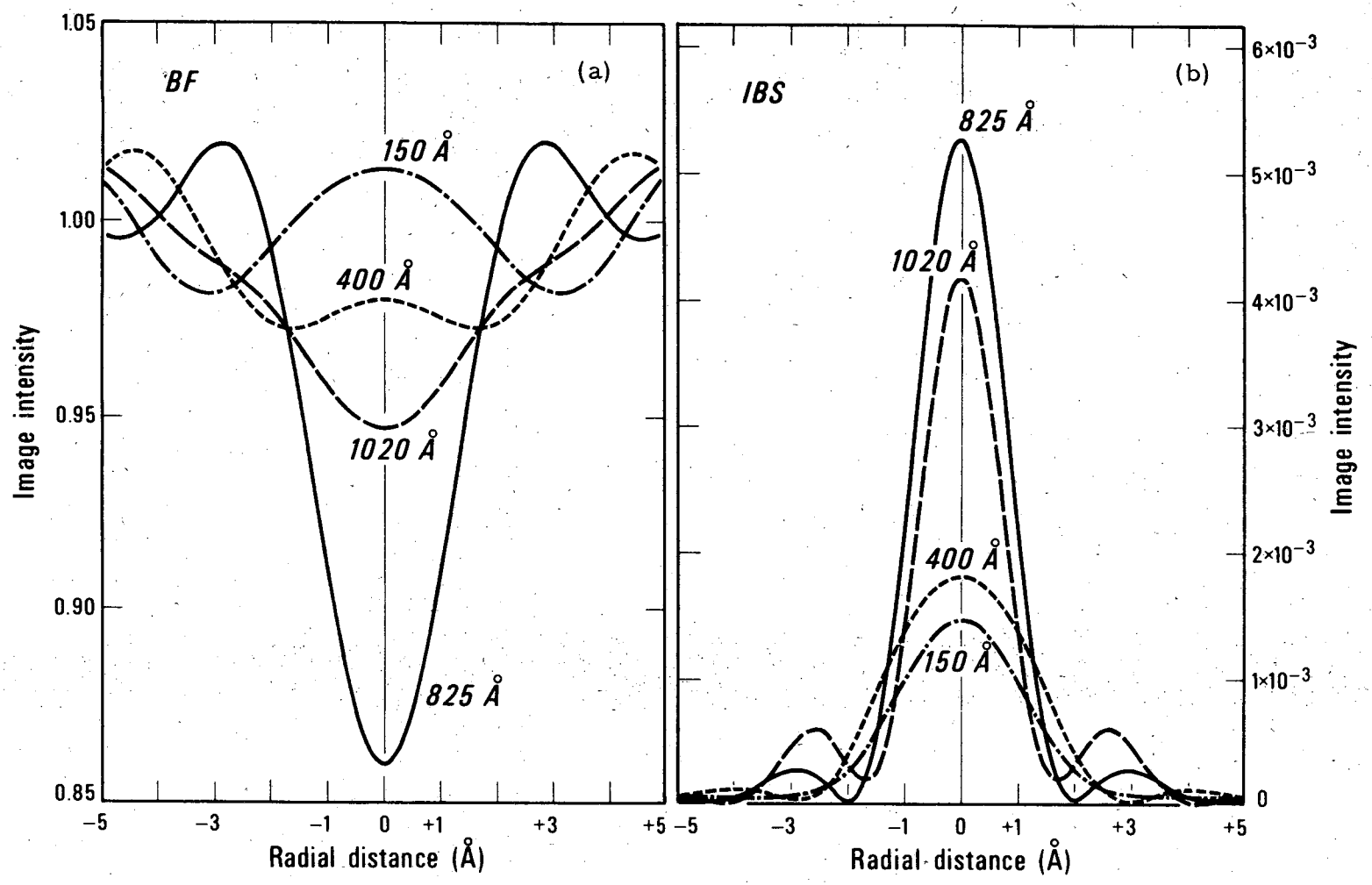

Figure 5

DBL 741-4608

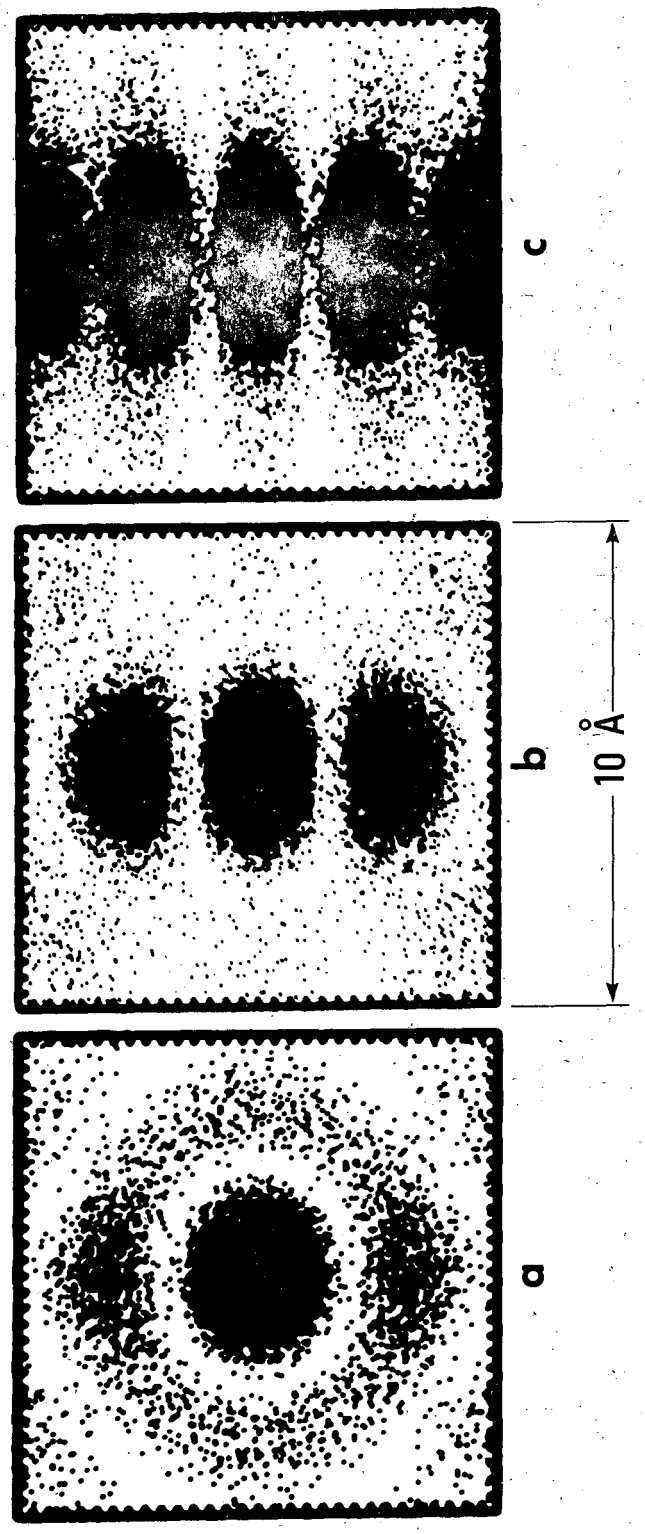

DBL 741-4604

Figure 6

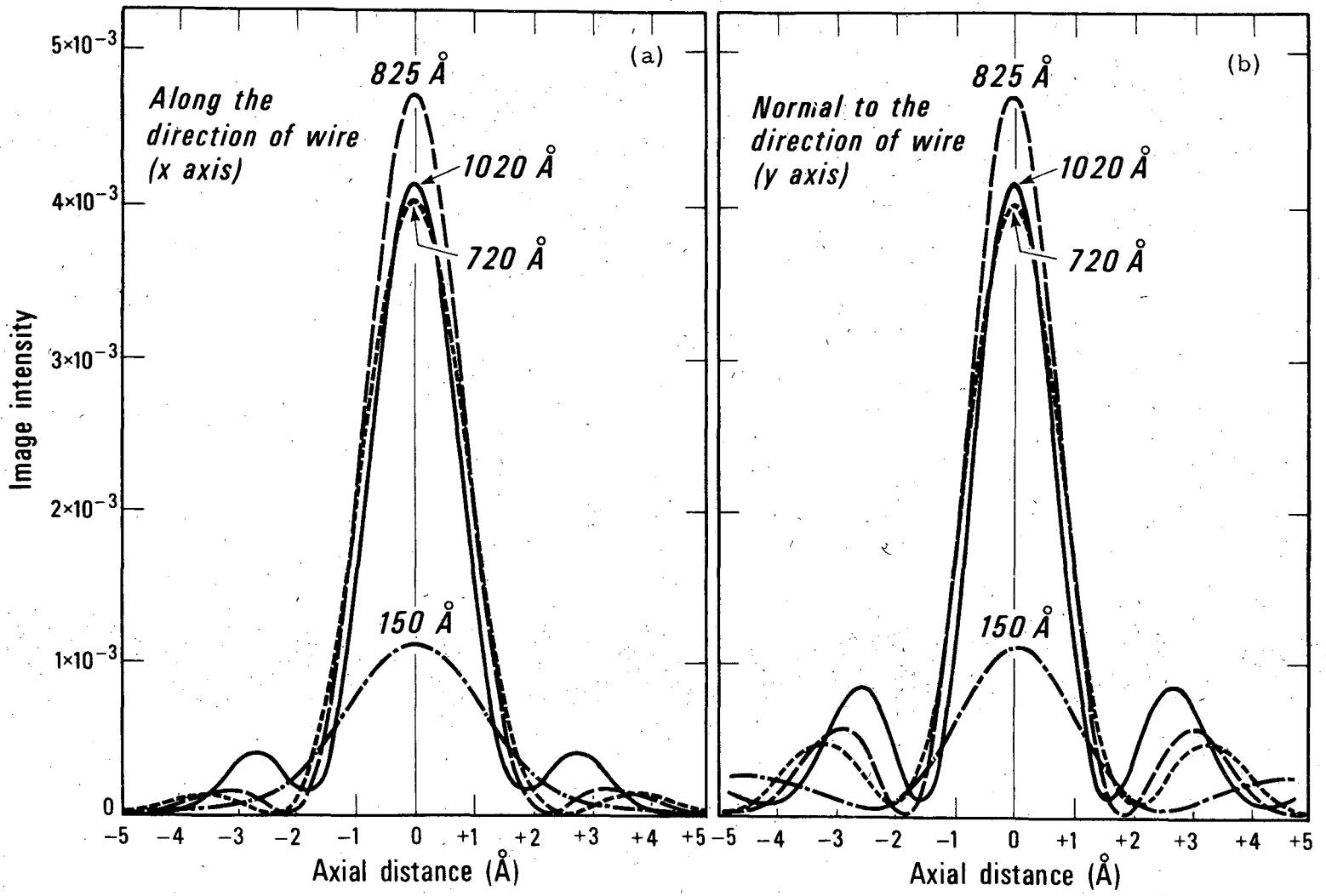

Figure 7

DBL 741-4607

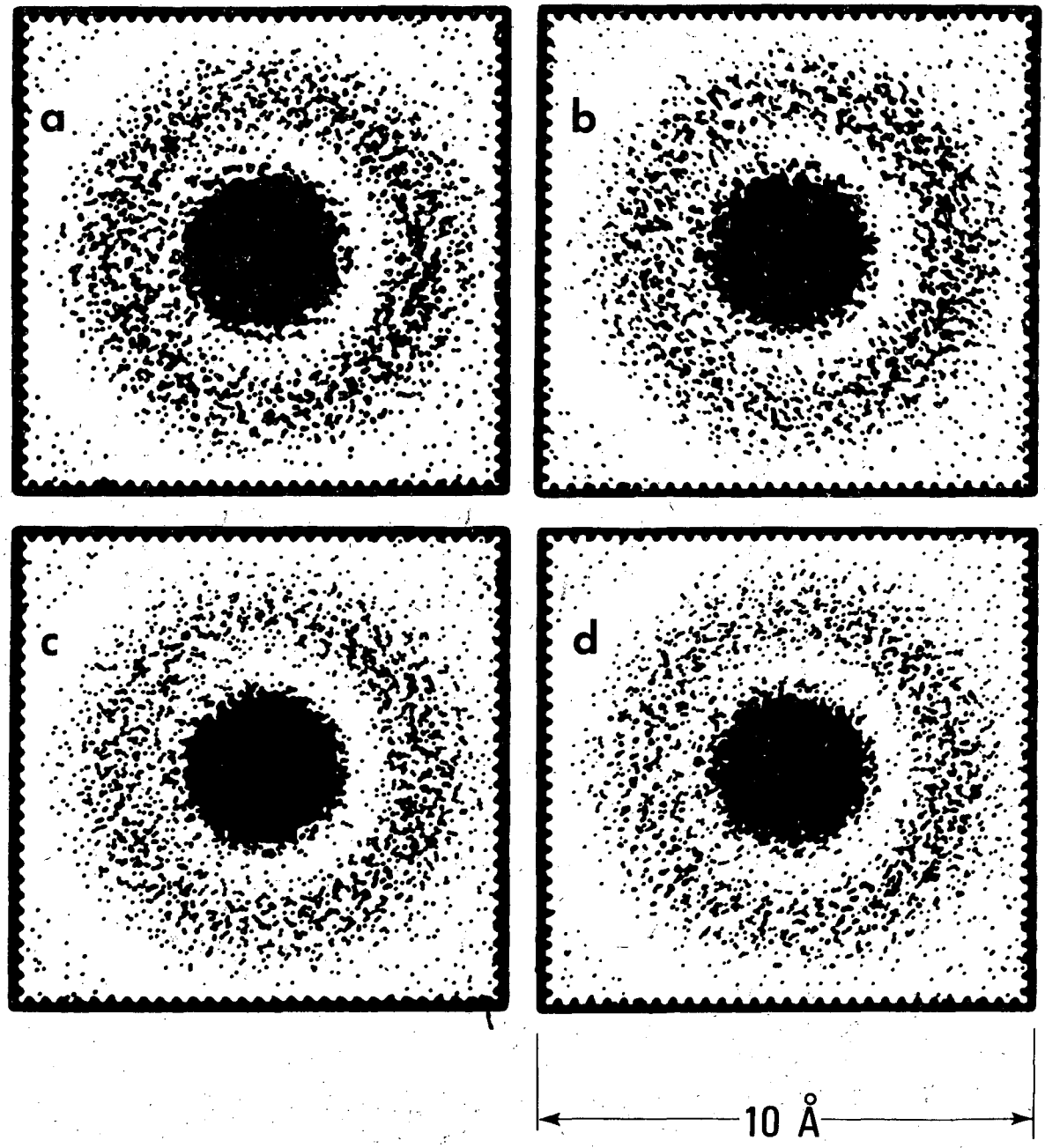

Figure 8

DBL 741-4605

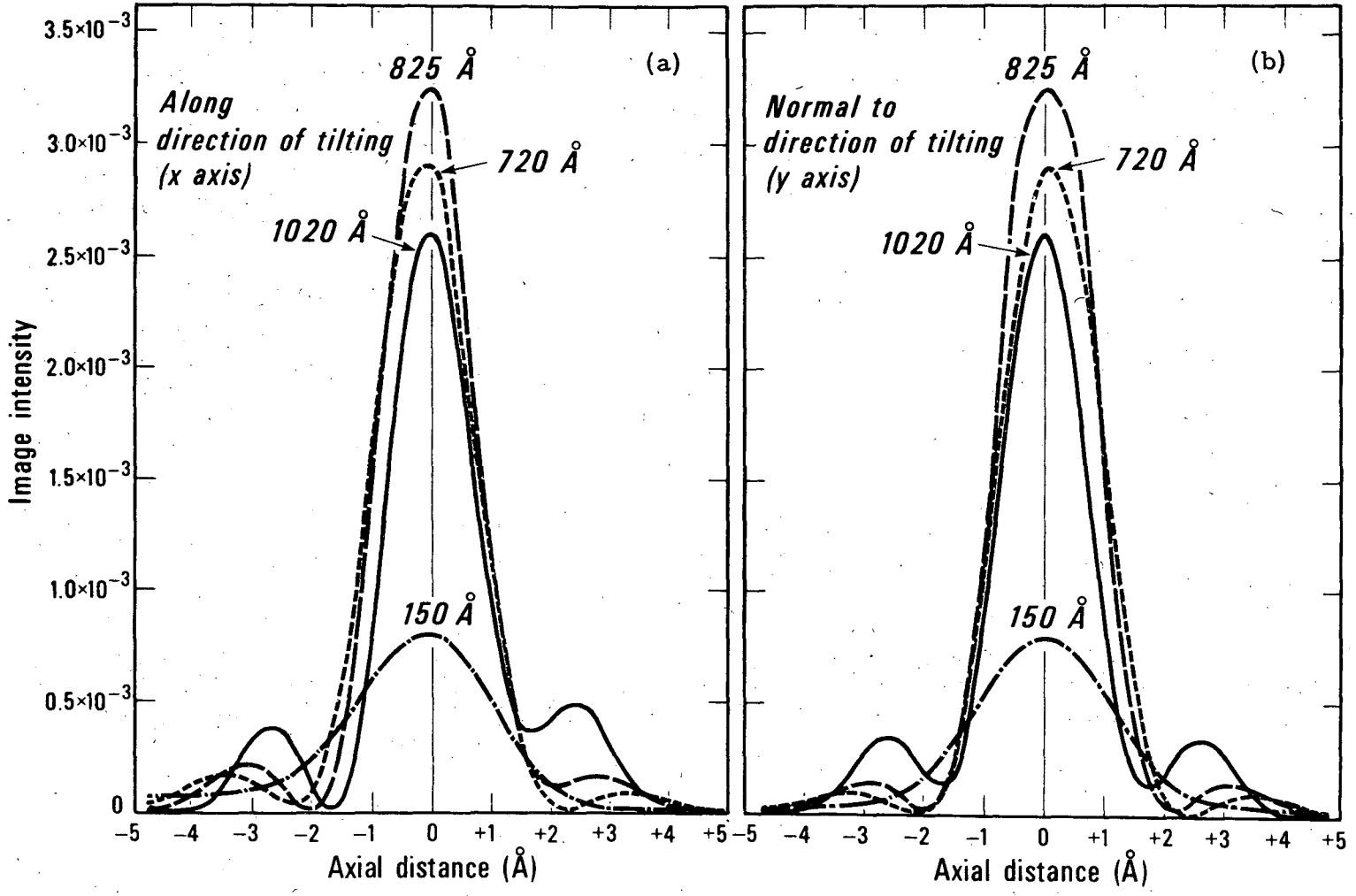

DBL 741-4606

Figure 9

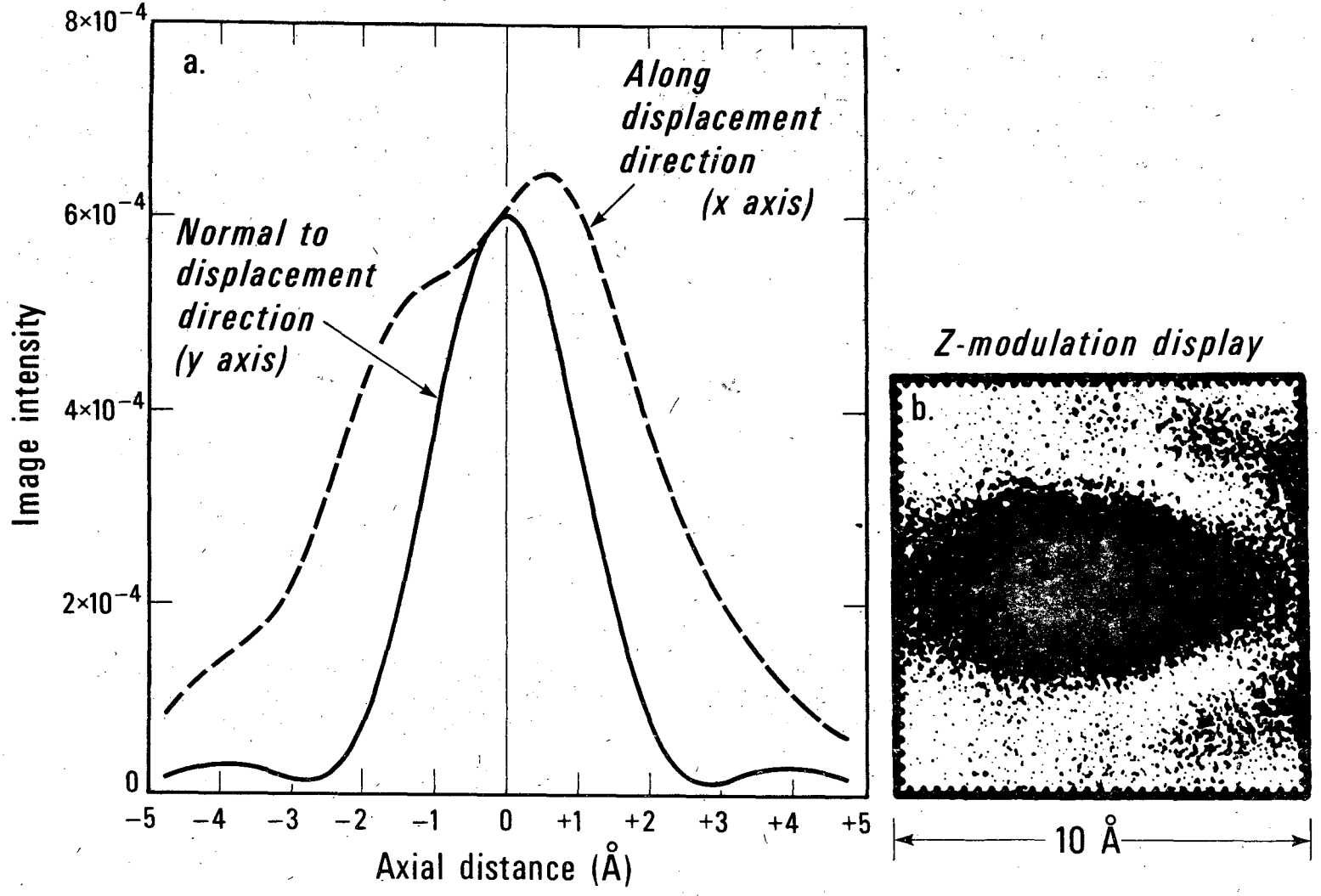

Figure 10

DBL 741-4603

TECHNICAL INFORMATION DIVISION
LAWRENCE BERKELEY LABORATORY
UNIVERSITY OF CALIFORNIA
BERKELEY, CALIFORNIA 94720